Journal of
*Marine Science and Engineering*

MDPI

*Article*

# Reconstructing Ocean Subsurface Temperature and Salinity from Sea Surface Information Based on Dual Path Convolutional Neural Networks

**Kai Mao [1], Chang Liu [1,2,*], Shaoqing Zhang [1,3,4] and Feng Gao [1,5]**

[1] College of Intelligent Systems Science and Engineering, Harbin Engineering University, Harbin 150001, China; maokai@hrbeu.edu.cn (K.M.); szhang@ouc.edu.cn (S.Z.); gaofeng19@hrbeu.edu.cn (F.G.)
[2] Qingdao Hatran Ocean Intelligence Technology Co., Ltd., Qingdao 266400, China
[3] Key Laboratory of Physical Oceanography, MOE, Institute for Advanced Ocean Study, Frontiers Science Center for Deep Ocean Multispheres and Earth System (DOMES), Ocean University of China, Qingdao 266100, China
[4] The College of Ocean and Atmosphere, Ocean University of China, Qingdao 266100, China
[5] Innovation and Development Center, Harbin Engineering University, Qingdao 266400, China
* Correspondence: liuchang407@hrbeu.edu.cn

**Abstract:** Satellite remote sensing can provide observation information of the sea surface, and using the sea surface information to reconstruct the subsurface temperature (ST) and subsurface salinity (SS) information has significant application values. This study proposes an intelligent algorithm based on Dual Path Convolutional Neural Networks (DP-CNNs) to reconstruct the ST and SS. The DP-CNN can integrate known information including sea surface temperature (SST), sea surface salinity (SSS), and sea surface height (SSH) to reconstruct the ST and SS. The reconstruction model based on DP-CNN can solve the problem of detail information loss in traditional CNN (Convolutional Neural Network) models. This study performs experiments for the South China Sea under different seasons using reanalysis data. The experimental results show that the DP-CNN models have higher reconstruction accuracy than the CNN models, and this proves that DP-CNNs effectively mitigate the loss of detailed information in the CNN models. Compared with the ground truth data, the ST/SS reconstruction results of the DP-CNN model exhibited a high coefficient of determination (0.93/0.86) and a low root mean square error (around 0.31 °C/0.05 PSU). Therefore, the DP-CNN models can be used as an effective approach to reconstruct ST and SS using sea surface information.

**Keywords:** dual path convolutional neural networks; deep learning; subsurface ocean temperature and salinity; satellite remote sensing observation

check for updates

**Citation:** Mao, K.; Liu, C.; Zhang, S.; Gao, F. Reconstructing Ocean Subsurface Temperature and Salinity from Sea Surface Information Based on Dual Path Convolutional Neural Networks. *J. Mar. Sci. Eng.* **2023**, *11*, 1030. https://doi.org/10.3390/jmse11051030

Academic Editors: Nikolaos Skliris and Jean-Louis Pinault

Received: 12 March 2023
Revised: 26 April 2023
Accepted: 9 May 2023
Published: 12 May 2023



## 1. Introduction

As human societies develop, the impact of the ocean on human life becomes more and more powerful. The earth stores most of its heat in the oceans, which therefore has a crucial influence on climate change [1,2]. In addition to this, fish aquaculture and offshore fishing are also affected by the changes of oceanic parameters. Therefore, accurately accessing oceanic parameters, especially the ocean temperature and salinity, is of great significance for climate monitoring and fisheries production.

However, due to the large size of the ocean and the limitations of human observations, we cannot directly access information on the three-dimensional (3D) temperature and salinity of the ocean. In our objective world, the geographic information that can be directly accessed is often limited. Until now, in situ observations of the oceans remain sparse. The only observations available, such as buoys, boat measurement, Expendable Bathythermograph (XBT), and underwater gliders, are very sparse and discontinuous in their spatial and temporal distribution. These observations have their own drawbacks that make them difficult to apply. At present, only satellite remote sensing methods are able to provide large-area ocean observations. The satellite can use sensors to carry out large-scale remote sensing observation of the state and change process of the ocean, and obtain remote sensing information of the sea surface with high spatial and temporal resolution, large coverage and long duration, solving the problem of uneven and discontinuous spatial distribution of observation data [3,4]. For example, satellites with microwave radiometers and thermal infrared sensors can observe sea surface temperature (SST), satellite altimeters can observe sea surface height (SSH), and SMAP (Soil Moisture Active Passive) satellites can provide observations of sea surface salinity (SSS). However, because electromagnetic waves cannot transmit effective information using seawater as a medium, these satellite remote sensing observations, whether active or passive, are limited to the sea surface and cannot directly access subsurface temperature (ST) and subsurface salinity (SS) information [5].

Based on known ocean dynamics, there are relationships between sea surface parameters and the subsurface thermohaline structure, so it is possible to use SST and SSS to reconstruct ST and SS [6–8]. In addition to SST and SSS, SSH is also strongly correlated with the subsurface thermohaline structure [9,10], because the SSH variations reflect the thermocline variations [11,12]. The above relationship pattern indicates that the constraint between the sea surface information and the subsurface information can be used to achieve ST and SS reconstruction. There have been numerous previous studies on techniques for subsurface information reconstruction using sea surface information. In general, the methods for subsurface information reconstruction include two main types: empirical analysis methods based on statistics and artificial intelligence methods based on neural networks.

The use of statistical models based on empirical analysis is the most common method for reconstruction. By analyzing the correlation between single or multiple elements in the historical data, using methods such as regression statistics, a statistical model of the correlation between surface and subsurface information can be developed. The reconstruction of ST and SS can then be conducted by inputting satellite remote sensing data into the statistical model. As early as 1983, Khedouri et al. [13] attempted to use satellite observations of SSH data to reconstruct the ST structure, and Cames et al. [14] used least squares regression to model the relationship between SSH and vertical structure of temperature in the Gulf of Mexico and reproduced the vertical structure of the Gulf Stream and eddies using the sea surface information. Chu et al. [15] showed that the ST structure can be determined directly from satellite SST observations by building a suitable statistical model. Fischer et al. [16] successfully estimated the vertical thermal structure of the equator using sea surface height anomalies (SSHA) and sea surface temperature anomalies (SSTA) based on a multivariate projection approach. The most widely used statistical model based on linear regression, the modular ocean data assimilation system (MODAS) [17], is currently one of the main tools used by the US Navy to obtain 3D ocean temperature and salinity information. Statistical methods have the advantage of high calculation speed, less computational resources required, and more flexible application. However, simple statistical methods lack the constraints of the dynamical equations, which leads to a low upper limit of accuracy for their inversion [18–21]. In addition, variational methods are also effective methods for performing the reconstruction of ST and SS [22].

In the field of geosciences, artificial intelligence techniques based on artificial neural networks (ANNs) have shown great potential to overcome limitations and improve the performance of related techniques [23]. ANNs methods have also been widely used to estimate and reconstruct ocean temperature, salinity, and other ocean variables [24–30]. The first to use neural networks to solve the ST reconstruction problem was Ali et al. [31], who initially used only the simplest fully connected ANN to reconstruct the ST using SST, SSH, wind stress, radiation, and heat flux as sea surface information, achieving a relatively impressive RMSE of 0.584 °C and $R^2$ of 0.85. Sammartino et al. [32] designed a multilayer perceptron (MLP) network to reconstruct a 3D temperature field. Lu et al. [33] combined a pre-clustering process with neural networks to estimate subsurface temperature anomalies

(STA) using ocean surface variables on a global scale. Han et al. [34] used a convolutional neural network (CNN) to estimate ST from satellite remote sensing observations. Su et al. [35] used a long short-term memory network (LSTM) to estimate STA and SSA (subsurface salinity anomalies). The reason for better reconstruction results from ANNs is their ability to more fully exploit the pattern information embedded in historical data and their ability to fit nonlinear mappings, which is not available from traditional statistical methods [36]. ANNs have become a powerful tool for describing correlations between the sea surface and subsurface parameters, and ANN-based reconstruction algorithms can quickly learn pattern features from the training dataset.

In general, there are three main types of ANN models commonly used: MLP, LSTM, and CNN. However, for the reconstruction problem of ST or SS, there are still some shortcomings in the principles of these models. Models using MLP and LSTM are weak at capturing spatial features while capturing spatial features of sea surface parameters is the key to the ST and SS reconstruction process. CNNs are able to capture spatial features better, but CNNs inevitably suffer from information loss during the convolution process, which might lose some of the key detailed features and lead to lower reconstruction accuracy.

To address the issues above, this study proposes a Dual Path Convolutional Neural Networks (DP-CNNs) model for ST and SS reconstruction using sea surface information. DP-CNN uses two information paths for convolutional computation, which can effectively mitigate the original detail information loss problem and improve reconstruction accuracy. Previous studies have investigated a variety of combined reconstruction schemes for sea surface parameters and have generally concluded that the combined schemes of SST, SSS, and SSH are the most representative. Therefore, this study will use SST, SSS, and SSH as the known sea surface information for the experiments on the reconstruction of ST and SS. To avoid the disturbance of errors caused by remote sensing data from different observation sources, this study will use reanalysis data from the same product system for the experiments, where SST, SSS, and SSH of the reanalysis data are used as simulated remote sensing observation information.

## 2. Materials and Methods

### *2.1. Data and Tools*

This experiment uses the monthly average reanalysis data as a training sample. The product from CMEMS (Copernicus Marine Environment Monitoring Service) has been integrated with global multi-source satellite remote sensing observations and in-situ ocean observations to provide a low level of error so that the sea surface data from this reanalysis dataset can be used to simulate satellite remote sensing observations to perform ST and SS reconstruction experiments. Available online: https://resources.marine.copernicus.eu/product-detail/MULTIOBS_GLO_PHY_TSUV_3D_MYNRT_015_012/INFORMATION (accessed on 6 June 2022). The dataset is in netCDF-4 format with a horizontal grid resolution of 1/4°. The experimental dataset has 45 layers in the vertical direction and a maximum water depth of 3000 m. The depth layer intervals are 0, 5, 10, 15, 20, 25, 30, 35, 40, 45, 50, 55, 60, 65, 70, 80, 90, 100, 125, 150, 175, 200, 225, 250, 275, 300, 350, 400, 450, 500, 550, 600, 700, 800, 900, 1000, 1100, 1200, 1300, 1400, 1500, 1750, 2000, 2500, 3000.

The experiment uses 23 years of reanalysis data from 1993–2015 as the training dataset and 3 years of reanalysis data from 2016–2018 as the simulated true values for testing. The scheme is as follows: the SST, SSS, and SSH from 1993–2015 are used as training samples, and the 44-layer ST and SS from 1993–2015 are used as training labels, respectively. Once the model training was completed, the ST and SS reconstruction results were obtained by inputting the SST, SSS, and SSH for 2016–2018 and the error evaluation was conducted using the 44-layer ST and SS for 2016–2018. The experiment was divided into four groups to examine the reconstruction effects under different seasons, respectively in March, June, September, and December.

The South China Sea was selected as the experimental area, and the experimental area is shown in Figure 1.

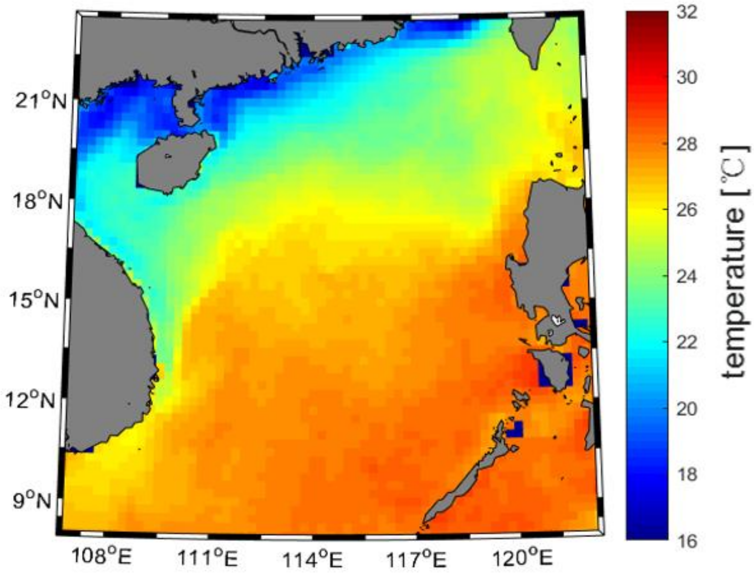


**Figure 1.** The experimental area—South China Sea. The SST data of March 2016 is used as an example for display.

The experimental data grid has a size of 64 × 64 in the horizontal direction and a depth range of 0–3000 m with 44 layers. Land region parameters in the data preprocessing will be filled with zero values. The ST and SS reconstructions from the four sets of experiments will be analyzed in comparison with the ST and SS from the 2016 reanalysis data and finally also compared with the reconstruction results of the original CNN model.

The ANN tool used in this study is Pytorch, which has been widely used in many scientific fields. Available online: https://pytorch.org/ (accessed on 10 October 2020).

### *2.2. Dual Path Convolutional Neural Networks*

The South China Sea is susceptible to typhoon transit, Kuroshio intrusion, and complex topography, all of which are frequently subject to mesoscale and sub-mesoscale processes. In addition, the seasonal oceanographic processes in the South China Sea also led to changes in the temperature and salt distribution structure. The temperature and salt parameters of the subsurface layer are closely related to the distribution characteristics of the sea surface element parameters. Therefore, it is crucial to capture the sea surface features for the problem of reconstructing the subsurface temperature and salt.

Referring to the previous studies, CNNs are the best model architecture for capturing spatial features [37]. Therefore, our study will be based on the CNN research route for improvement. CNNs are very good at processing matrixed data, which can be read directly without spreading and can use convolutional kernels as sliding filters to extract and capture spatial features of the gridded data. The training parameters are reduced by convolutional kernels and pooling operations, which allows the processing of larger-scale gridded data with limited computational resources. Therefore, CNNs can effectively capture feature relationships between neighboring grid points with less demand on computational resources.

Convolution in general reduces the gridded data to a smaller matrix size without losing the key features. However, in the reconstruction process, in addition to the key features, other detailed information may also have some influence on the reconstruction accuracy, so a simple convolution operation may end up having some impact on the accuracy of the ST and SS reconstruction due to the loss of detailed information. This requires the model to be able to extract features while retaining detailed information, so the information flow path of the CNN must be changed to satisfy the requirements.

Based on the idea of U-net architecture [38], the solution is to change the CNN to a dual path information flow, where one path performs convolutional computation at the original size to avoid loss of detailed information, and the other path performs feature extraction and dimensionality reduction with pooling operations, which are used to save computational resources and increase computational speed. Finally, the two path information streams are converged and then convolved. To highlight the role of dual path convolution in the reconstructing process, it is named Dual Path Convolutional Neural Network (DP-CNN).

The schematic architecture of DP-CNN is shown in Figure 2.

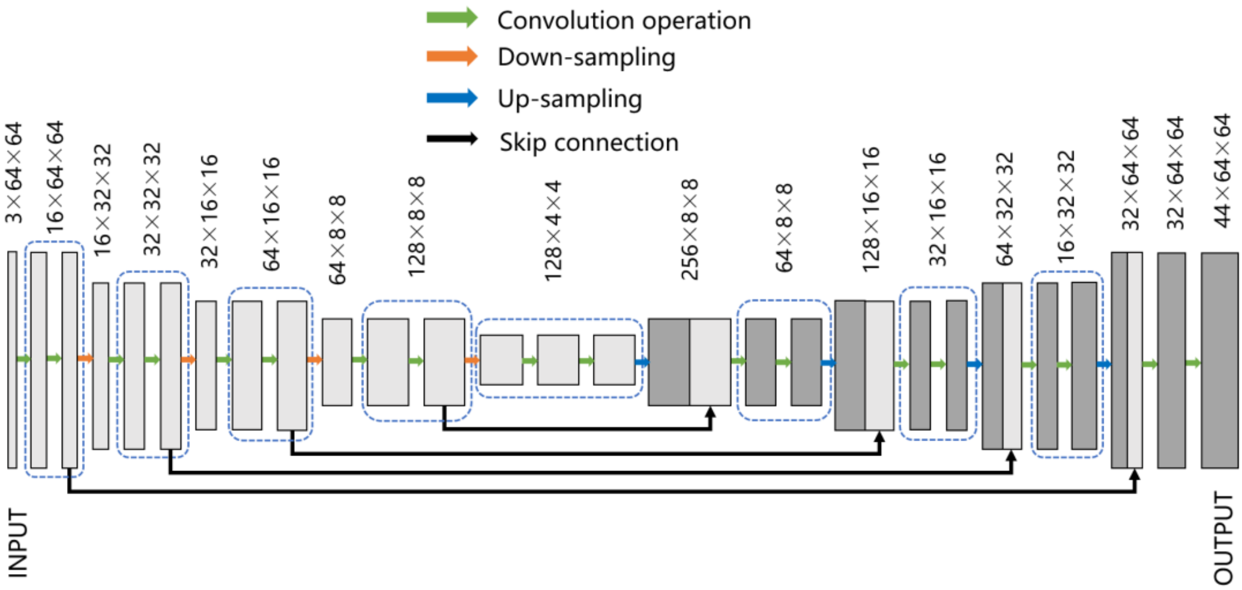


**Figure 2.** The schematic architecture of DP-CNN.

Each convolution layer consists of a convolution operation, a batch normalization operation, and a ReLU activation function. The down-sampling is Average Pooling operations, and the up-sampling is bi-linear interpolation. In theory, Average Pooling can retain more background information and overall features of the matrix data, while Max Pooling can retain more matrix textural information that is suitable for tasks such as image recognition. Therefore, the DP-CNN model for ST and SS reconstruction uses the Average Pooling scheme.

As shown in Figure 2, before each down-sampling, the original matrix information is retained until the final convolution process using skip connections and combined with the up-sampled feature matrix for another convolution calculation, thus retaining the original matrix information while extracting the feature information. The problem of detailed information loss in traditional CNN models will be effectively solved by the DP-CNN.

Taking the temperature reconstruction as an example, the two convolutions for the input variables can be expressed as:

$$DoubleConv(x) = ReLU[BN[w_2 * [ReLU(BN(w_1 * x + b_1))] + b_2]] \quad (1)$$

where $w$ is the convolution kernel weight, $*$ represents the convolution operation, $b$ is the bias, $BN$ is the batch normalization, and $ReLU$ is the nonlinear activation function.

In Figure 2, the input data is the combined SST, SSS, and SSH sea surface parameter matrix S, whose matrix size is $3 \times 64 \times 64$; it becomes a $16 \times 64 \times 64$ 3D feature matrix S1 by double convolution:

$$\mathrm{S1} = DoubleConv(\mathrm{S}) \quad (2)$$

This feature matrix S1 will flow to two different paths: one path is down sampled, reduced by a factor of 2 in the number of horizontal grids by a pooling operation to 16 × 32 × 32, and changed by double convolution to a feature matrix S2 of 32 × 32 × 32:

$$\text{S2} = DoubleConv(DownSampling(\text{S1})) \tag{3}$$

The feature matrix S2 continues to flow into two different paths: one for down sampling, shrinking the number of horizontal grids by a factor of 2 through pooling operations to 32 × 16 × 16, and changing to a 64 × 16 × 16 feature matrix S3 through double convolution:

$$\text{S3} = DoubleConv(DownSampling(\text{S2})) \tag{4}$$

The feature matrix S3 continues to flow into two different paths: one for down sampling, shrinking the number of horizontal grids by a factor of 2 through pooling operations to 64 × 8 × 8, and changing to a 128 × 8 × 8 feature matrix S4 through double convolution:

$$\text{S4} = DoubleConv(DownSampling(\text{S3})) \tag{5}$$

The feature matrix S4 continues to flow into two different paths: one is down sampled, reduced by a factor of 2 in the number of horizontal grids by pooling operations, and turned into a 128 × 4 × 4 feature matrix S5 by double convolution outputs:

$$\text{S5} = DoubleConv(DownSampling(\text{S4})) \tag{6}$$

The feature matrix S4 is another jump connection, and the feature matrix S5 is combined with the feature matrix S4 after up sampling, forming a 256 × 8 × 8 feature matrix and becoming the feature matrix S6 by double convolution:

$$\text{S6} = DoubleConv(UpSampling(\text{S5})\,|\text{S4}) \tag{7}$$

The other strip of feature matrix S3 is a jump connection, and feature matrix S6 is combined with feature matrix S3 after up sampling to form a 128 × 16 × 16 feature matrix and turned into feature matrix S7 by double convolution:

$$\text{S7} = DoubleConv(UpSampling(\text{S6})\,|\text{S3}) \tag{8}$$

The feature matrix S2 is another jump connection, and the feature matrix S7 is combined with the feature matrix S2 after up sampling, forming a 64 × 32 × 32 feature matrix and becoming the feature matrix S8 by double convolution:

$$\text{S8} = DoubleConv(UpSampling(\text{S7})\,|\text{S2}) \tag{9}$$

Feature matrix S1 another for jump connection, feature matrix S8 after up sampling and feature matrix S1 combined to form a 32 × 64 × 64 feature matrix and by double convolution, the output result is the subsurface temperature field ST:

$$\text{ST} = DoubleConv(UpSampling(\text{S8})\,|\text{S1}) \tag{10}$$

In this way, a nonlinear mapping relationship between the sea surface information S and the subsurface temperature field ST is established by DP-CNN:

$$\text{ST} = DoubleConv\big(UpSampling\big(f'(\text{S})\big)|DoubleConv(\text{S})\big) \tag{11}$$

where $f'$ represents the feature extraction process for S, | is the matrix merging symbol.

The reconstruction of salinity follows the same pattern. From the above equation, we can see that with DP-CNN, the sea surface element parameters can directly affect the temperature and salt distribution in the subsurface layer. Through the dual path of

DP-CNN, the features are extracted, and the information loss problem is mitigated, which makes the reconstruction accuracy of the temperature and salt improved.

The neural network parameters were set as follows: The convolution kernel size is 3 × 3, the training epoch was set to 1000, the initial learning rate was 0.001, the batch size value was 12, and the convolutional layers were 26 in total, including 4 down-samples and 4 up-samples.

In the experiments of this paper, the evaluation criteria used in this paper are the root mean square error (RMSE) and the coefficient of determination ($R^2$). The formulae are as follows:

$$RMSE = \sqrt{\frac{\sum_{i=1}^{p}(m_i - a_i)^2}{p}}, \tag{12}$$

$$R^2 = 1 - \frac{\sum_{i=1}^{p}(a_i - m_i)^2}{\sum_{i=1}^{p}(a_i - a_{mean})^2}, \tag{13}$$

where $m$ is the reconstruction results, $a$ is the truth data, $p$ is the number of all grid data, and $a_{mean}$ is the mean value of all truth data.

## 3. Results

### *3.1. Temperature*

In order to test the reconstruction effectiveness of the DP-CNN model, this paper uses the model to estimate the temperature at 44 depths in the South China Sea respectively. Based on previous studies, it was found that reconstruction errors at deeper layers are usually small. Therefore, in order to show a visible reconstruction effect, the representative water depths of 50 m and 200 m were taken to evaluate the results of the estimated temperature spatial distribution.

Figures 3–10 present the comparison of the estimated temperature data by the DP-CNN model and the ground truth data for 2016–2018, where the first row is the ground truth data, and the second row is the estimated temperature data.

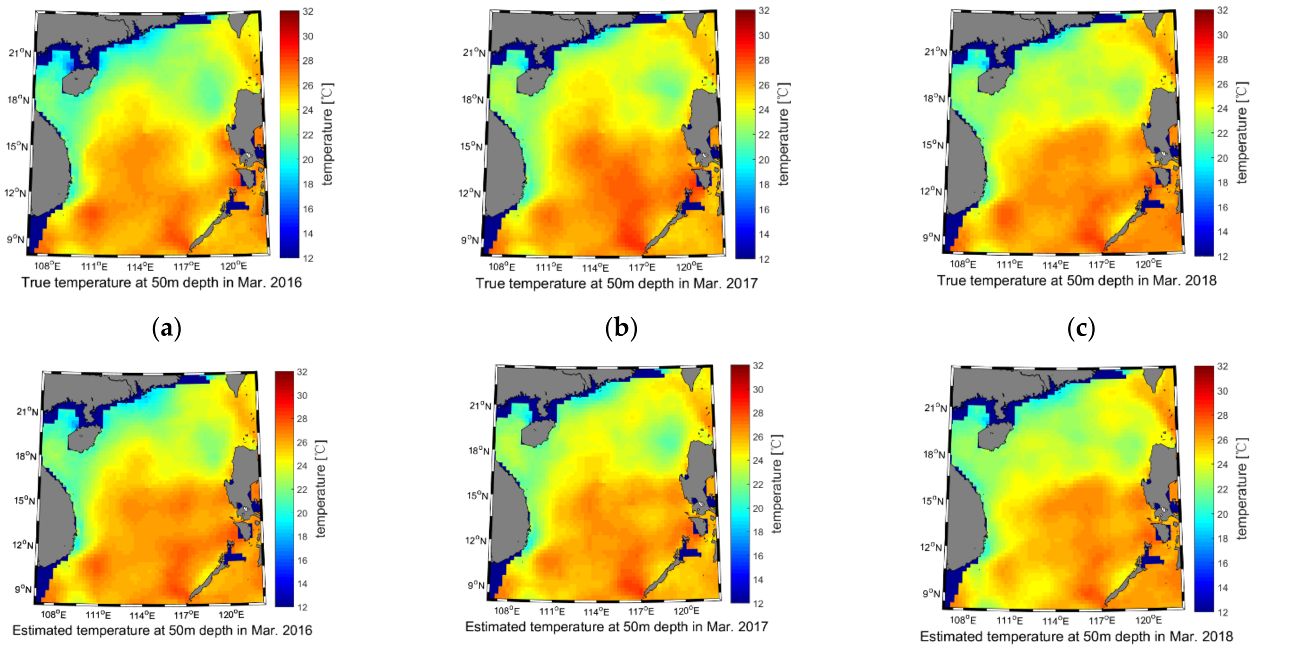


(**a**) (**b**) (**c**)

(**d**) (**e**) (**f**)

**Figure 3.** Temperature reconstruction results of the 50 m water depth for March 2016–2018. (**a**) True temperature of 2016; (**b**) True temperature of 2017; (**c**) True temperature of 2018; (**d**) Estimated temperature of 2016; (**e**) Estimated temperature of 2017; (**f**) Estimated temperature of 2018.

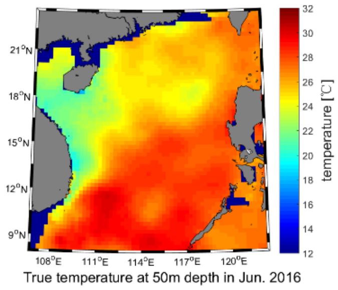


(**a**)

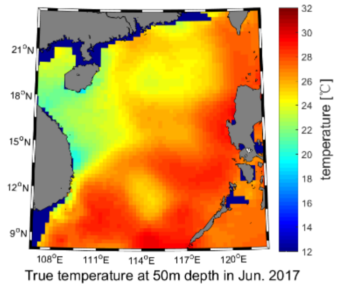


(**b**)

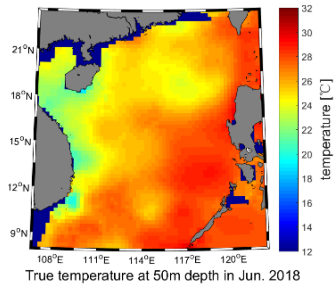


(**c**)

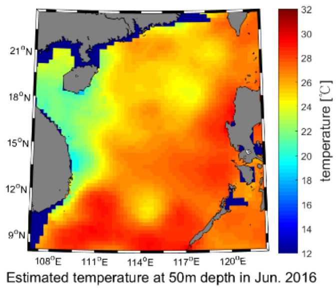


(**d**)

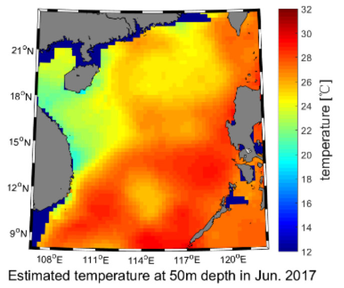


(**e**)

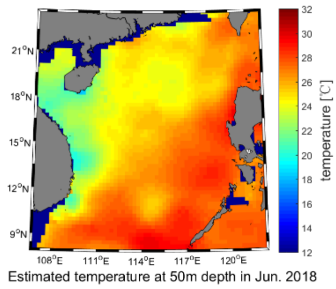


(**f**)

**Figure 4.** Temperature reconstruction results of the 50 m water depth for June 2016–2018. (**a**) True temperature of 2016; (**b**) True temperature of 2017; (**c**) True temperature of 2018; (**d**) Estimated temperature of 2016; (**e**) Estimated temperature of 2017; (**f**) Estimated temperature of 2018.

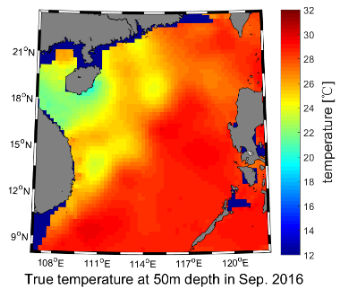


(**a**)

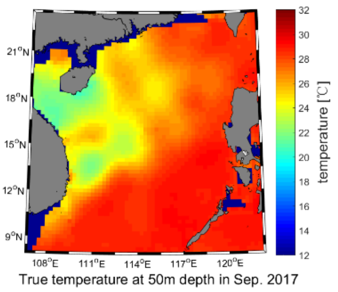


(**b**)

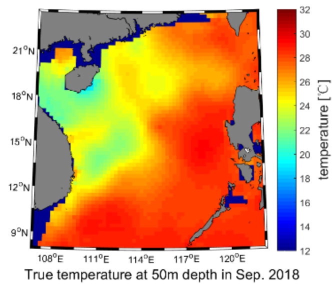


(**c**)

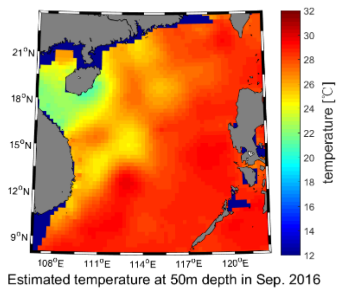


(**d**)

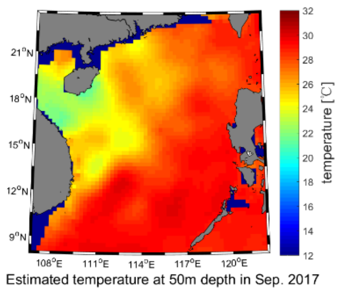


(**e**)

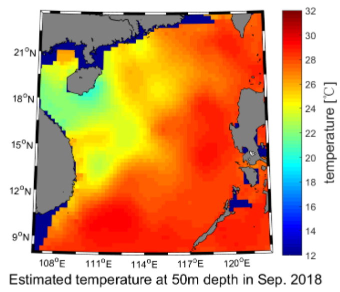


(**f**)

**Figure 5.** Temperature reconstruction results of the 50 m water depth for September 2016–2018. (**a**) True temperature of 2016; (**b**) True temperature of 2017; (**c**) True temperature of 2018; (**d**) Estimated temperature of 2016; (**e**) Estimated temperature of 2017; (**f**) Estimated temperature of 2018.

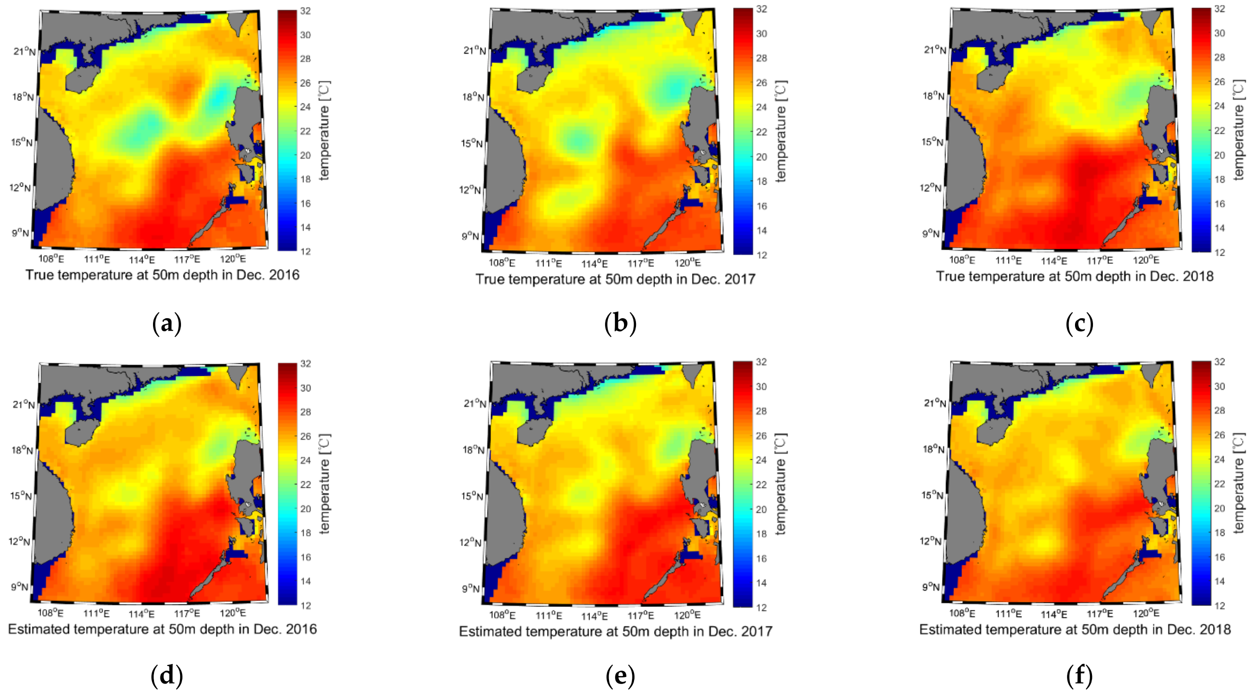


**Figure 6.** Temperature reconstruction results of the 50 m water depth for December 2016–2018. (**a**) True temperature of 2016; (**b**) True temperature of 2017; (**c**) True temperature of 2018; (**d**) Estimated temperature of 2016; (**e**) Estimated temperature of 2017; (**f**) Estimated temperature of 2018.

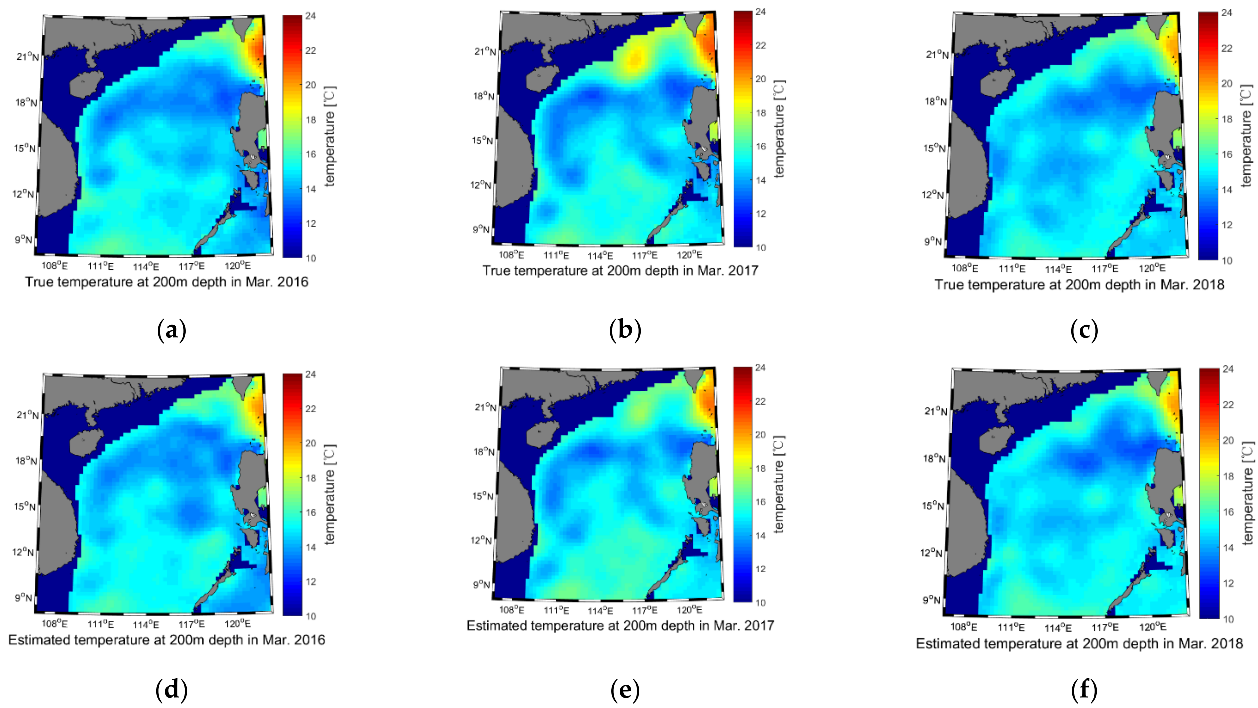


**Figure 7.** Temperature reconstruction results of the 200 m water depth for March 2016–2018. (**a**) True temperature of 2016; (**b**) True temperature of 2017; (**c**) True temperature of 2018; (**d**) Estimated temperature of 2016; (**e**) Estimated temperature of 2017; (**f**) Estimated temperature of 2018.

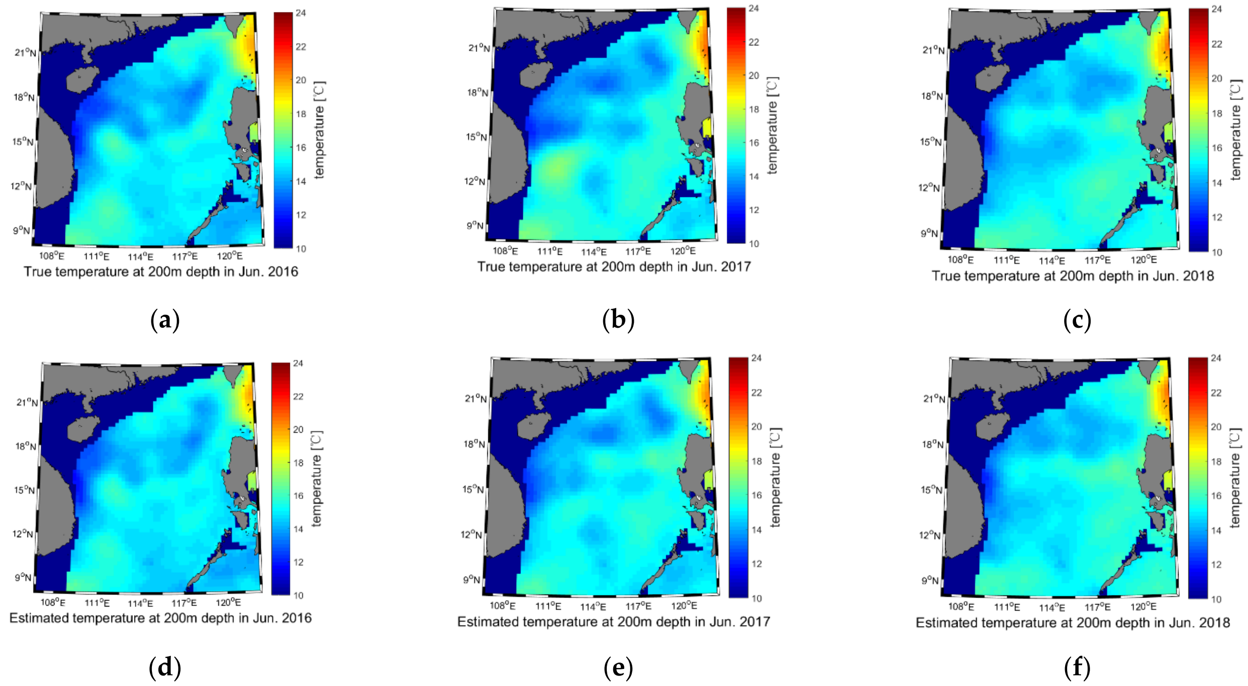


**Figure 8.** Temperature reconstruction results of the 200 m water depth for June 2016–2018. (**a**) True temperature of 2016; (**b**) True temperature of 2017; (**c**) True temperature of 2018; (**d**) Estimated temperature of 2016; (**e**) Estimated temperature of 2017; (**f**) Estimated temperature of 2018.

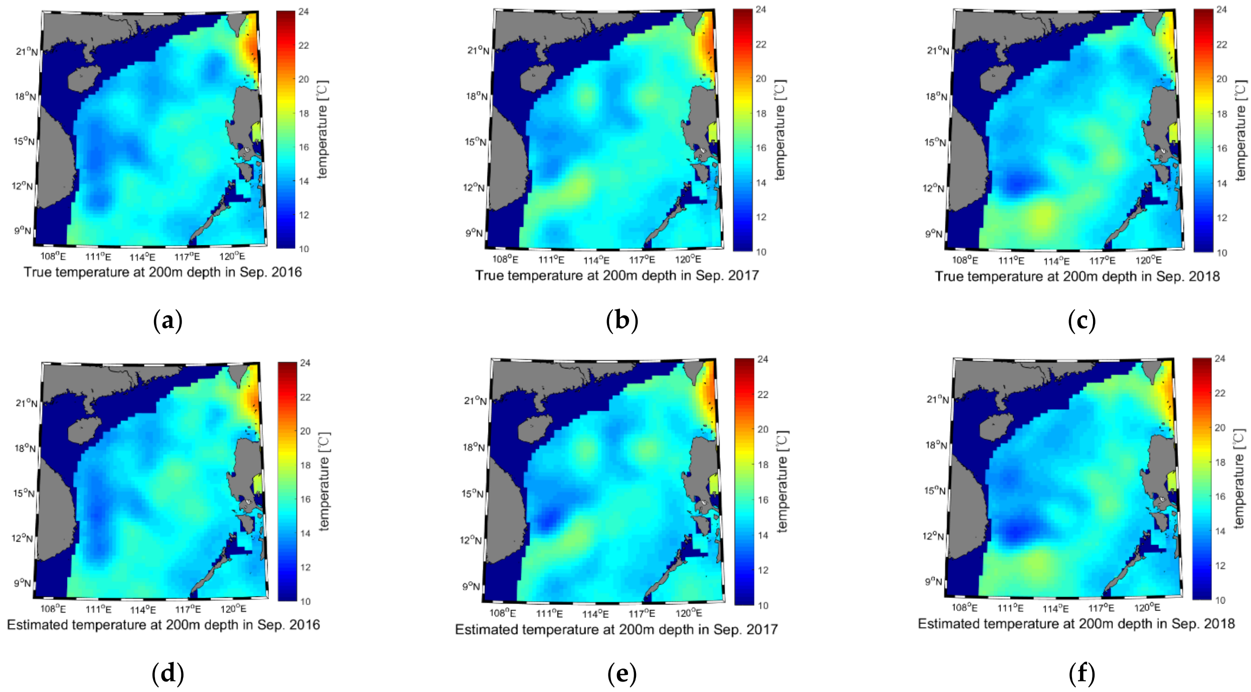


**Figure 9.** Temperature reconstruction results of the 200 m water depth for September 2016–2018. (**a**) True temperature of 2016; (**b**) True temperature of 2017; (**c**) True temperature of 2018; (**d**) Estimated temperature of 2016; (**e**) Estimated temperature of 2017; (**f**) Estimated temperature of 2018.

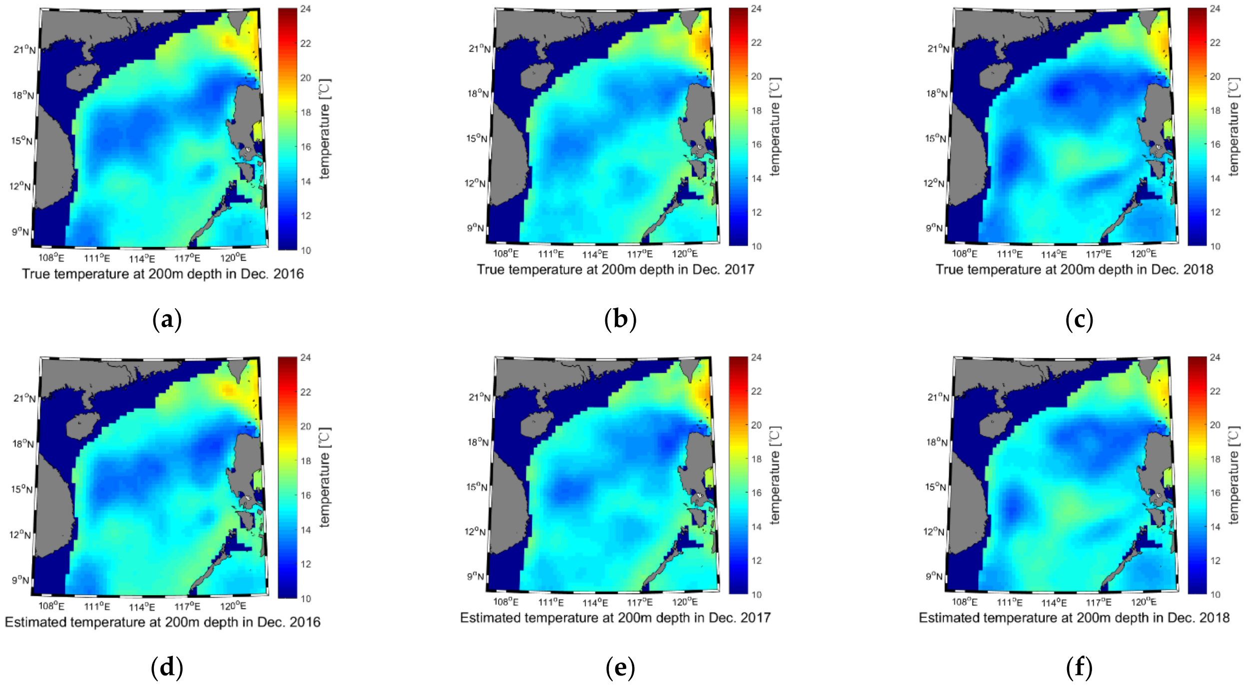


**Figure 10.** Temperature reconstruction results of the 200 m water depth for December 2016–2018. (**a**) True temperature of 2016; (**b**) True temperature of 2017; (**c**) True temperature of 2018; (**d**) Estimated temperature of 2016; (**e**) Estimated temperature of 2017; (**f**) Estimated temperature of 2018.

The water depth of 50 m in the South China Sea is about near the junction of the mixed layer and thermocline, which can represent the upper ocean. As shown in Figures 3–6, the spatial distribution of the estimated temperature field by the DP-CNN model at 50 m depth are in general consistent with the spatial distribution of the true temperature field. For example, the reconstructed temperature field is closer to the true value field for the distinctive cold eddies in the northern South China Sea in June and September. As can be seen from the above figure, the reconstruction errors in the second half of the year are larger than those in the first half, especially in December. However, the errors in most regions are small and the noticeable errors emerge only in the partial areas, which are mostly caused by the drastic changes of weather conditions. When there are drastic changes of weather conditions, the upper ocean tends to deviate from the historical pattern. For example, in December 2016, a typhoon crossing over the South China Sea resulted in large fluctuations of upper ocean temperatures. This ultimately causes an increase in the local deviation of the reconstructed temperature compared with the truth temperature.

The water depth of 200 m in the South China Sea is about near the deeper thermocline, which can represent the thermocline ocean. Figures 7–10 show the 200 m water depth reconstruction results. As can be seen from Figures 7–10, the reconstructed temperature distribution structure at 200 m depth is generally accurate. Such as the more complex temperature distribution structure in the central South China Sea for 2018 in Figure 7, the DP-CNN model can clearly reconstruct it all. The location and size of the warm eddies in Figures 7c,d and 8b,e are nearly identical. This suggests that the model makes full use of known sea surface information and learns the correlation patterns from the vertically constrained relationships of ocean parameters present in the historical data. As can be seen in Figure 10, the temperature at 200 m water depth is not as obviously affected by typhoons as it is at 50 m water depth, and the overall reconstructions for 200 m water depth are more accurate. Comparing the reconstruction results for 2016, 2017, and 2018, it was found that the best reconstructions were produced for 2016. This is possibly due to the fact that 2016 is the nearest time to the training sample. The closer the time, the greater the correlation of the pattern.

Having analyzed the spatial characteristics of the reconstruction results above, the vertical distribution of the errors should be analyzed next. Figure 11 plots the reconstruction errors at different depths for the four seasonal months to show the structural characteristics of the vertical error distribution. The evaluation metrics used are RMSE and $R^2$. The vertical error results from RMSE show that the errors are mainly concentrated in the upper layers of the ocean, including the mixed layer and the thermocline, with errors ranging from 0.2 °C to 1.0 °C. The errors in the deeper layers are generally smaller, basically less than 0.2 °C. This is because deep-sea temperature fluctuations are small and regular, and regularity is easy to grasp for the DP-CNN model, which can achieve good results at small error levels. In terms of seasonality, the reconstruction errors are larger for the depth layer above 100 m in December. As analyzed earlier, this is an extreme effect caused by the crossing of typhoons, which can reduce the temperature of the upper layers within the sea area by 5–6 °C, with a cooling range of up to 100 km in diameter. The vertical structure of temperature in the South China Sea changes markedly after the typhoon's transit. In terms of the vertical errors in the figure, the reconstructions for March, June, and September are better, with smaller reconstruction errors and a maximum RMSE error of less than 0.7 °C. From the vertical distribution of $R^2$, the reconstructions of the mixed layer and the deep layer are better and basically close to the truth value field, while the reconstructions of the thermocline have lower $R^2$ due to high volatility, with the smallest $R^2$ occurring in December.

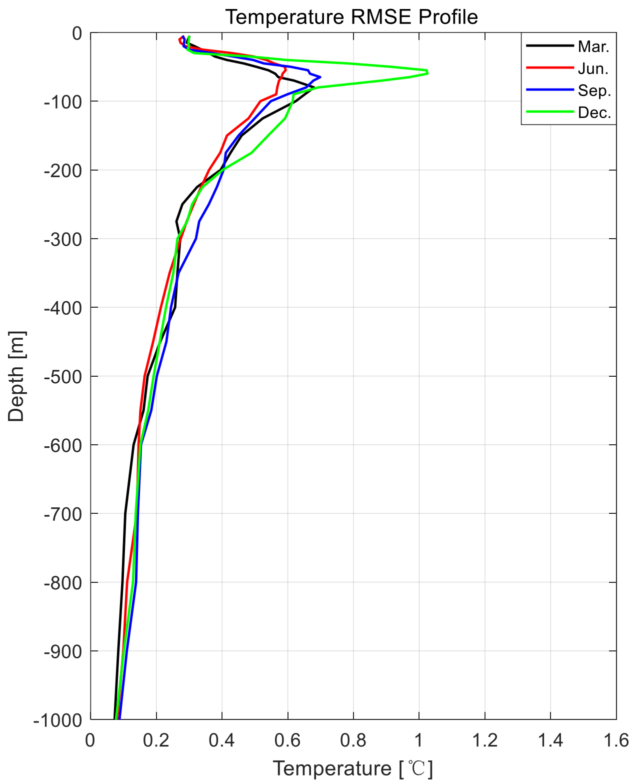


(a)

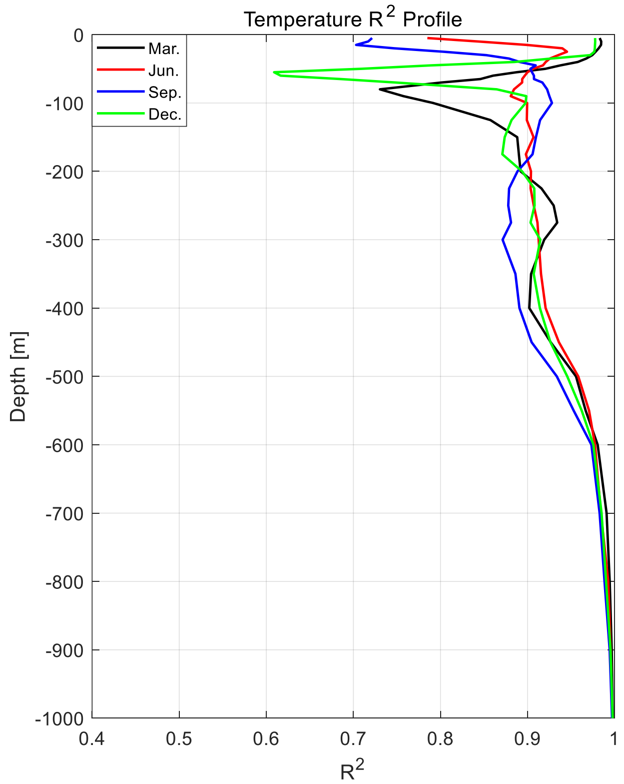


(b)

**Figure 11.** RMSE and $R^2$ results of temperature for 2016–2018: (**a**) 3-year average RMSE for 4 months; (**b**) 3-year average $R^2$ for 4 months. The RMSE and $R^2$ count all grid points for each depth layer.

The effectiveness of DP-CNN has been proven above by comparison with the ground truth data, and the reconstruction results will be compared with that of the traditional CNN model in the following. Table 1 shows the overall RMSE and $R^2$ results for each experimental group. It can be found from the experimental results that the DP-CNN effectively improves the reconstruction accuracy. The results show that the DP-CNN model has a much smaller reconstruction error. In each month of the experiment, the DP-CNN model outperformed the reconstructions of the CNN model. The DP-CNN model exhibited a lower RMSE of 0.31 °C, with a 0.05 °C reduction relative to the CNN model. The DP-CNN model also exhibited a higher $R^2$ of 0.93, with an improvement of 0.05 relative to the CNN model.

**Table 1.** RMSE and $R^2$ of reconstructed temperature. The RMSE and $R^2$ in the table are the average values of RMSE and $R^2$ for each layer.

| Evaluation Criteria | Method | March | June | September | December | Mean |
|---|---|---|---|---|---|---|
| RMSE | CNN | 0.36 | 0.34 | 0.36 | 0.39 | 0.36 |
| | DP-CNN | 0.29 | 0.29 | 0.31 | 0.35 | 0.31 |
| $R^2$ | CNN | 0.88 | 0.90 | 0.83 | 0.89 | 0.88 |
| | DP-CNN | 0.94 | 0.94 | 0.91 | 0.91 | 0.93 |

### 3.2. Salinity

The reconstruction errors for salinity are much smaller in order of magnitude compared with that for temperature. Figures 12–19 present the comparison of the estimated salinity data by the DP-CNN model and the ground truth data for 2016–2018, where the first row is the ground truth data, and the second row is the estimated salinity data.

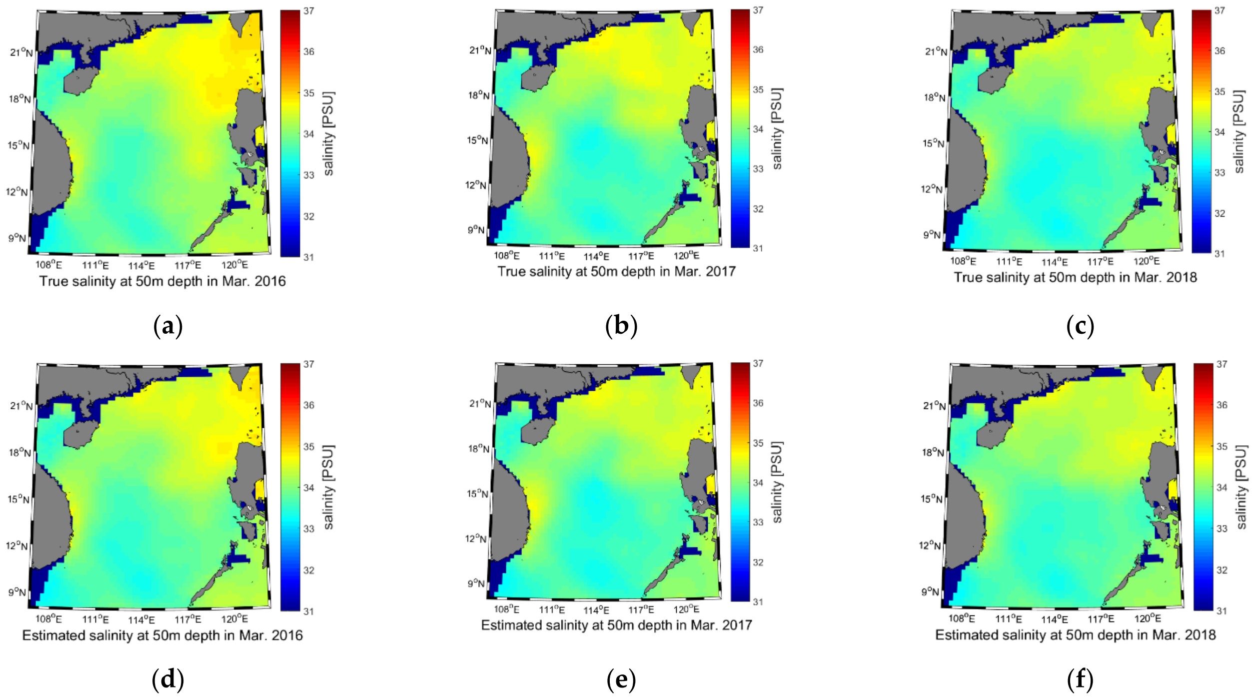


**Figure 12.** Salinity reconstruction results of the 50 m water depth for March 2016–2018. (**a**) True salinity of 2016; (**b**) True salinity of 2017; (**c**) True salinity of 2018; (**d**) Estimated salinity of 2016; (**e**) Estimated salinity of 2017; (**f**) Estimated salinity of 2018.

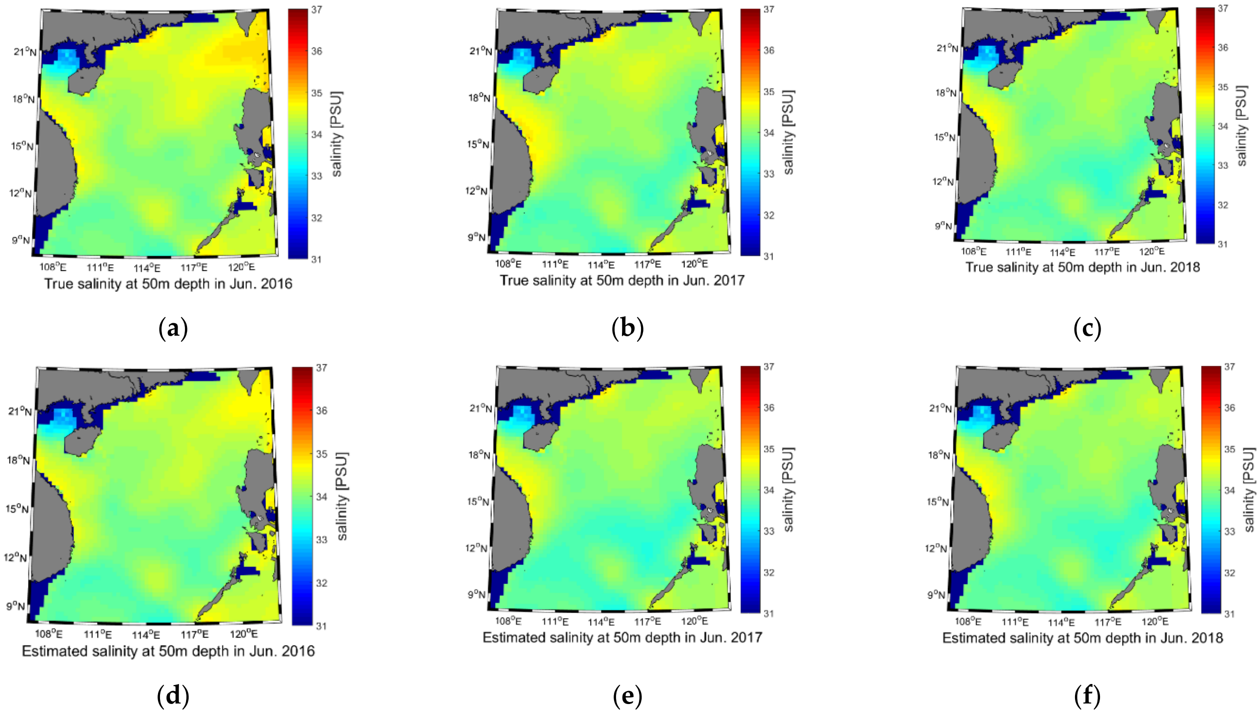


**Figure 13.** Salinity reconstruction results of the 50 m water depth for June 2016–2018. (**a**) True salinity of 2016; (**b**) True salinity of 2017; (**c**) True salinity of 2018; (**d**) Estimated salinity of 2016; (**e**) Estimated salinity of 2017; (**f**) Estimated salinity of 2018.

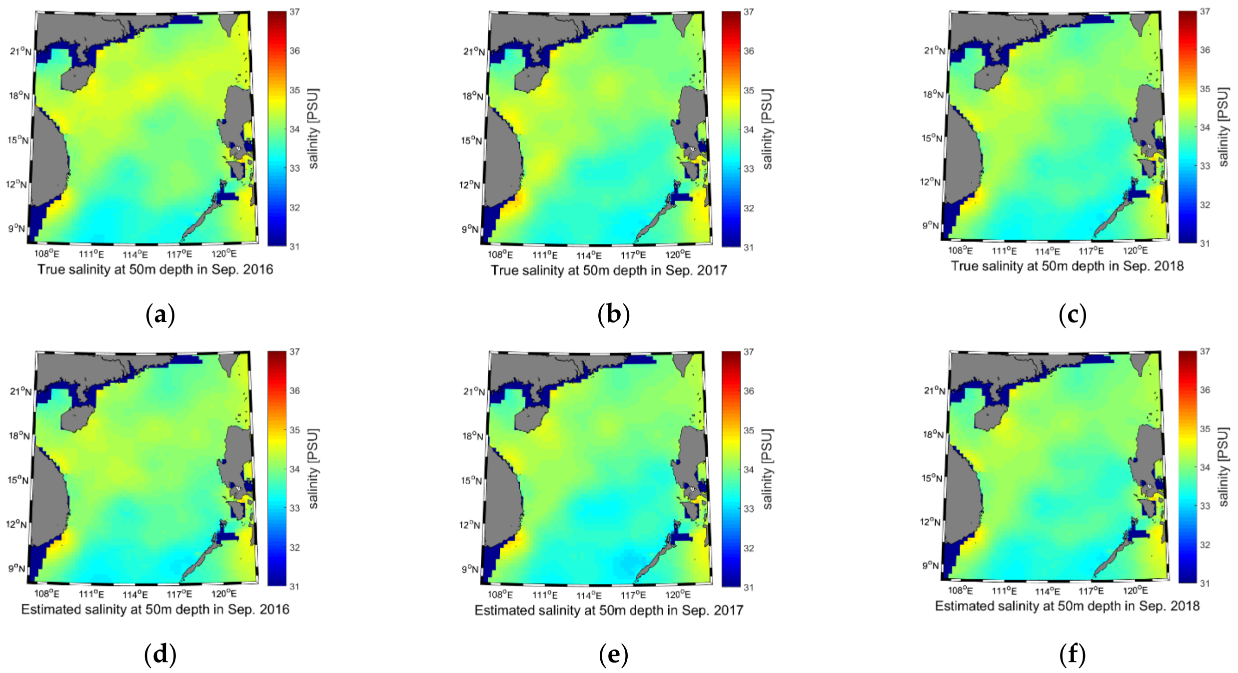


**Figure 14.** Salinity reconstruction results of the 50 m water depth for September 2016–2018. (**a**) True salinity of 2016; (**b**) True salinity of 2017; (**c**) True salinity of 2018; (**d**) Estimated salinity of 2016; (**e**) Estimated salinity of 2017; (**f**) Estimated salinity of 2018.

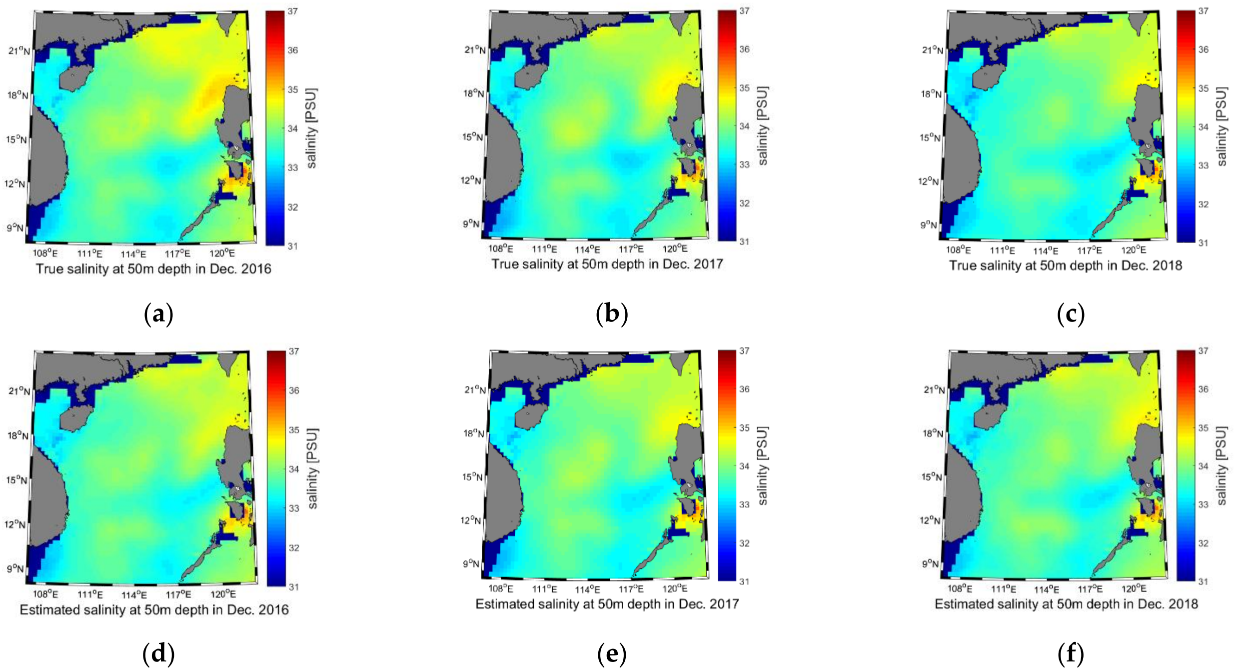


**Figure 15.** Salinity reconstruction results of the 50 m water depth for December 2016–2018. (**a**) True salinity of 2016; (**b**) True salinity of 2017; (**c**) True salinity of 2018; (**d**) Estimated salinity of 2016; (**e**) Estimated salinity of 2017; (**f**) Estimated salinity of 2018.

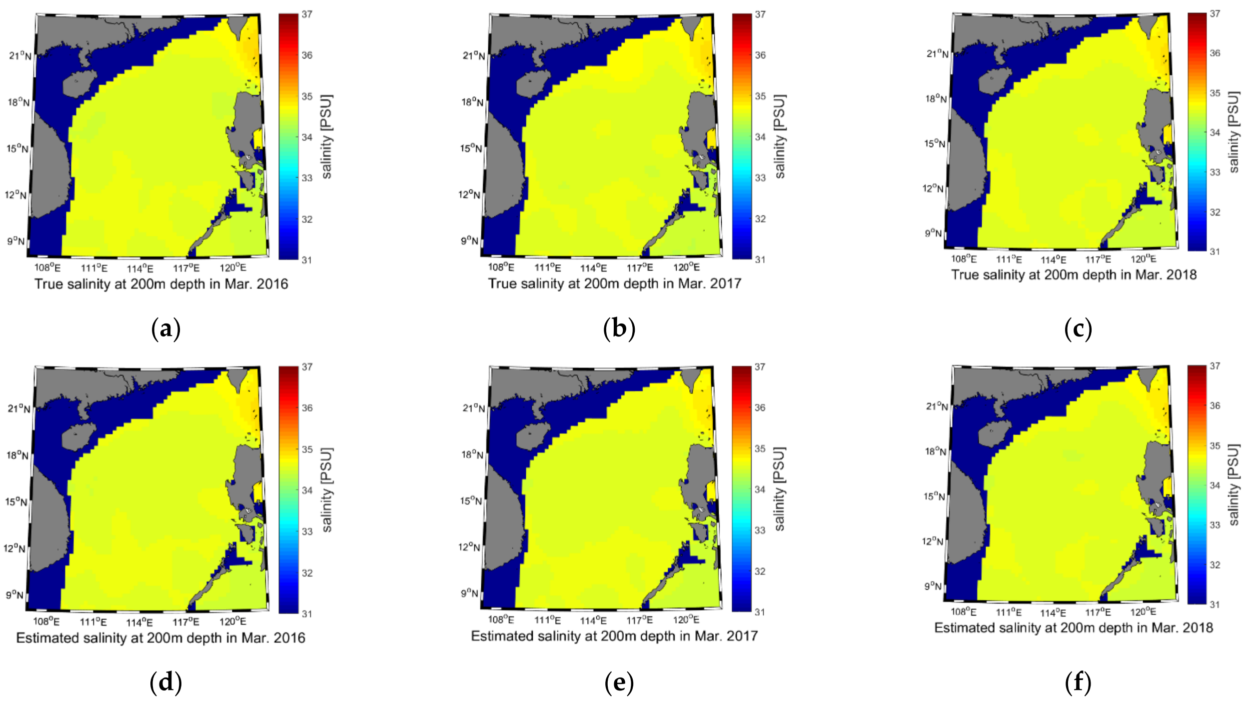


**Figure 16.** Salinity reconstruction results of the 200 m water depth for March 2016–2018. (**a**) True salinity of 2016; (**b**) True salinity of 2017; (**c**) True salinity of 2018; (**d**) Estimated salinity of 2016; (**e**) Estimated salinity of 2017; (**f**) Estimated salinity of 2018.

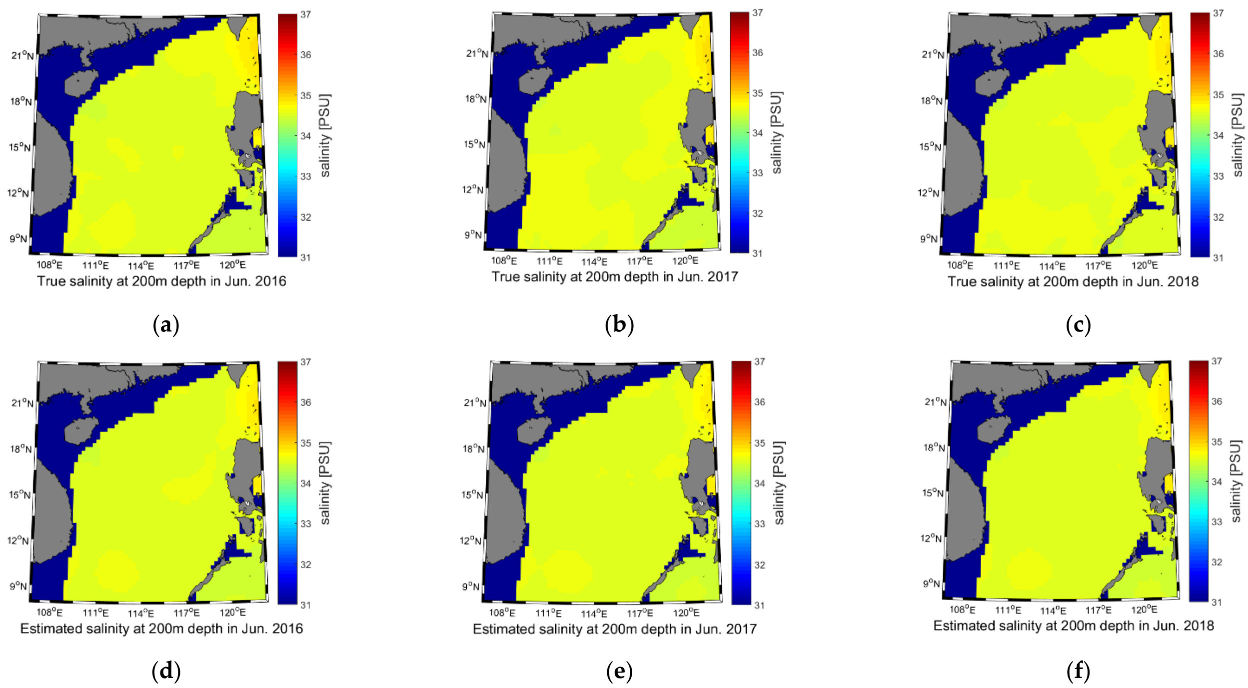


**Figure 17.** Salinity reconstruction results of the 200 m water depth for June 2016–2018. (**a**) True salinity of 2016; (**b**) True salinity of 2017; (**c**) True salinity of 2018; (**d**) Estimated salinity of 2016; (**e**) Estimated salinity of 2017; (**f**) Estimated salinity of 2018.

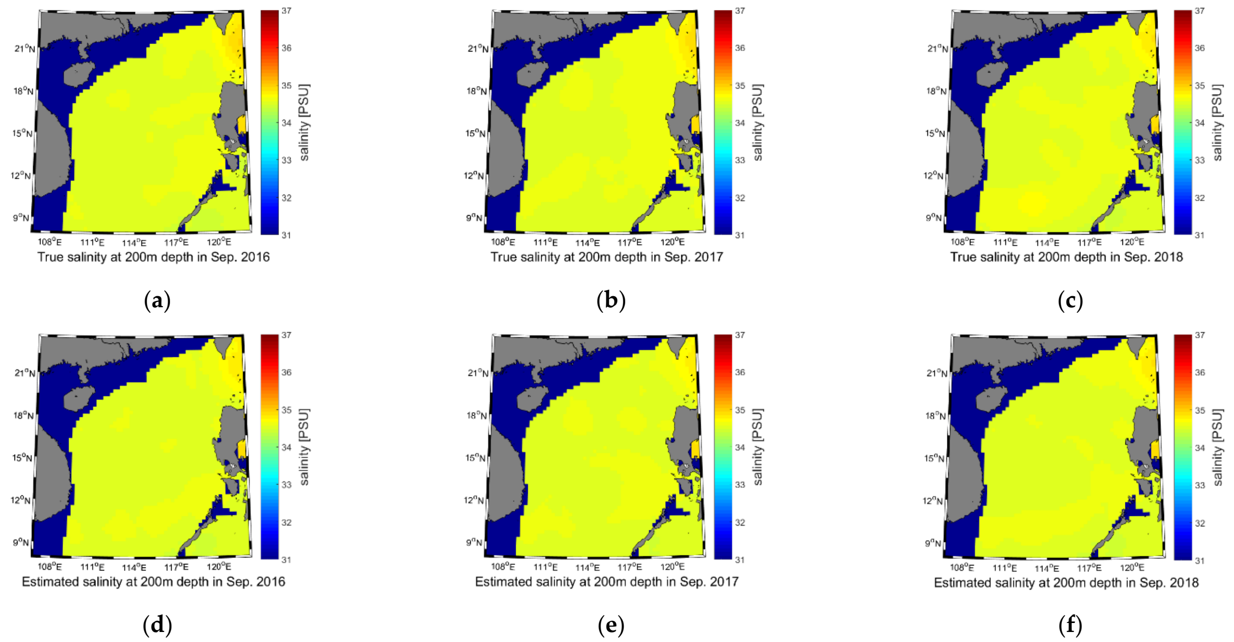


**Figure 18.** Salinity reconstruction results of the 200 m water depth for September 2016–2018. (**a**) True salinity of 2016; (**b**) True salinity of 2017; (**c**) True salinity of 2018; (**d**) Estimated salinity of 2016; (**e**) Estimated salinity of 2017; (**f**) Estimated salinity of 2018.

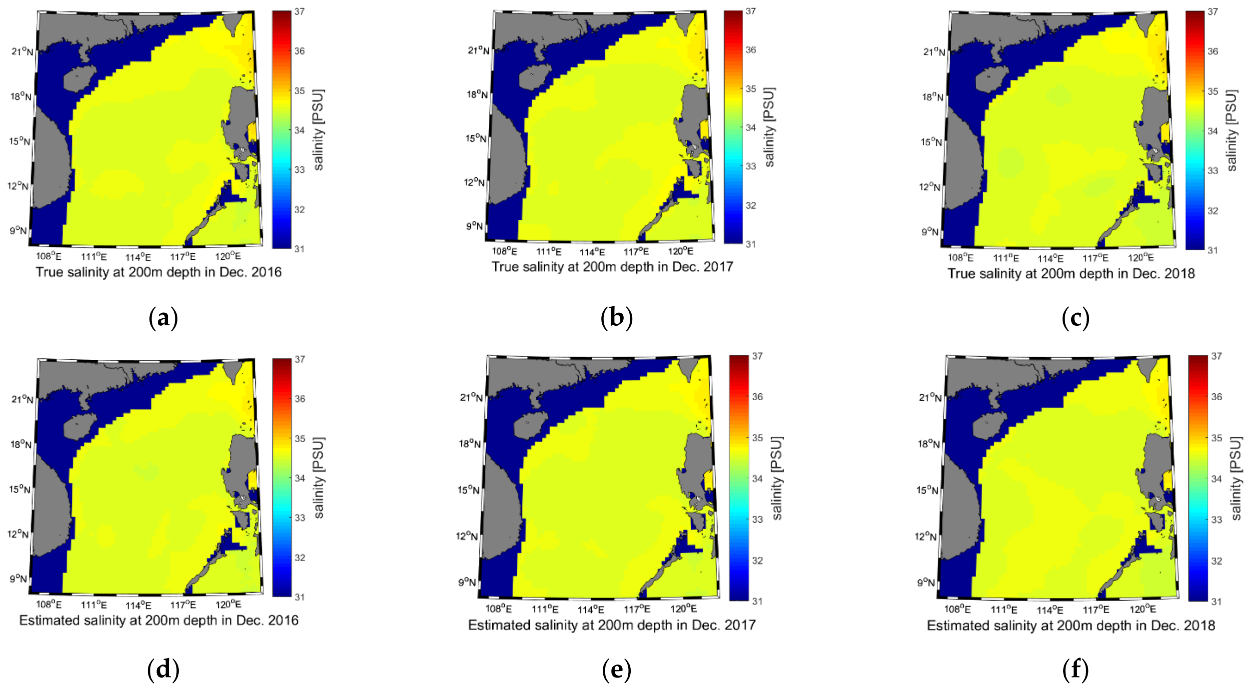


**Figure 19.** Salinity reconstruction results of the 200 m water depth for December 2016–2018. (**a**) True salinity of 2016; (**b**) True salinity of 2017; (**c**) True salinity of 2018; (**d**) Estimated salinity of 2016; (**e**) Estimated salinity of 2017; (**f**) Estimated salinity of 2018.

As shown in Figures 12–15, the spatial distribution of the estimated salinity field by the DP-CNN model at 50 m depth is in general consistent with the spatial distribution of the true salinity field. As can be seen from the above figure, the errors in most regions are small and the noticeable errors emerge only in the partial areas. The Luzon Strait Branch in the figure shows more noticeable reconstruction errors in March and June of 2016, which may be due to the variation of the Kuroshio Current. This also indicates that reconstructions are usually better for regular steady-state areas and more difficult for areas susceptible to disturbances from external factors. As previously mentioned, the impact of a typhoon that crossed over in December 2016 has resulted in a relatively noticeable error in the northeastern South China Sea, as shown in Figure 15d. Typhoon crossing would cause the salinity in the upper ocean to increase, so the reconstructed salinity results would be smaller than the true values. In general, the 50 m salinity reconstruction results are relatively accurate when not disturbed by typhoons and other factors, and the results of the DP-CNN model are generally consistent with the actual structural characteristics of the salinity distribution. Even if there are errors, they are local and only numerical.

The results of the salinity reconstructions for 200 m water depth are shown next. Figures 16–19 show the 200 m water depth reconstruction results of salinity. As shown in the figure, the reconstructed salinity distribution structure at 200 m depth is generally accurate. The reconstruction error at 200 m water depth is smaller compared to 50 m water depth. This is because 200 m depth is less influenced by atmospheric forces and the salinity distribution is more stable, making it easier to capture the vertical distribution pattern by deep learning. As can be seen from the figure, although there was the effect of a typhoon crossing in December, it did not have a noticeable effect on the salinity at 200 m water depth, so all three sets of experimental results are basically more accurate.

The spatial characteristics of the reconstruction results were analyzed above, and next the vertical error distribution profile of the salinity reconstructions will be analyzed. Figure 20 shows the RMSE and $R^2$ results for 2016–2018. Reconstruction errors are plotted separately for the four seasonal months at different depths to show the structure of the vertical error distribution. The vertical error results for RMSE show that it is similar to the temperature error distribution results that errors are mainly concentrated in the upper ocean, including the mixed layer and thermocline, with salinity reconstruction errors ranging from 0.02 PSU to 0.15 PSU. The errors in the deep ocean are particularly low, generally less than 0.02 PSU. This is because the deep ocean salinity fluctuations are small and regular, and the regularity is easily captured by the DP-CNN, allowing good reconstruction results to be achieved with a small order of magnitude for error. The RMSE shows that the reconstruction accuracy of December salinity was not obviously affected by the typhoon. The vertical error in the figure shows that the reconstructions are good for all four months, with the reconstruction errors being small and not exceeding 0.15 PSU. The vertical distribution of $R^2$ shows that only the mixed layer has good reconstruction effects, while the thermocline salinity has relatively small $R^2$ reconstruction results. The minimum $R^2$ for the upper layer occurs in June, probably due to the high summer precipitation and evaporation. Unlike temperature, there is a decreasing trend in $R^2$ with increasing depth, indicating that the correlation between deep layer salinity and sea surface parameters has weakened.

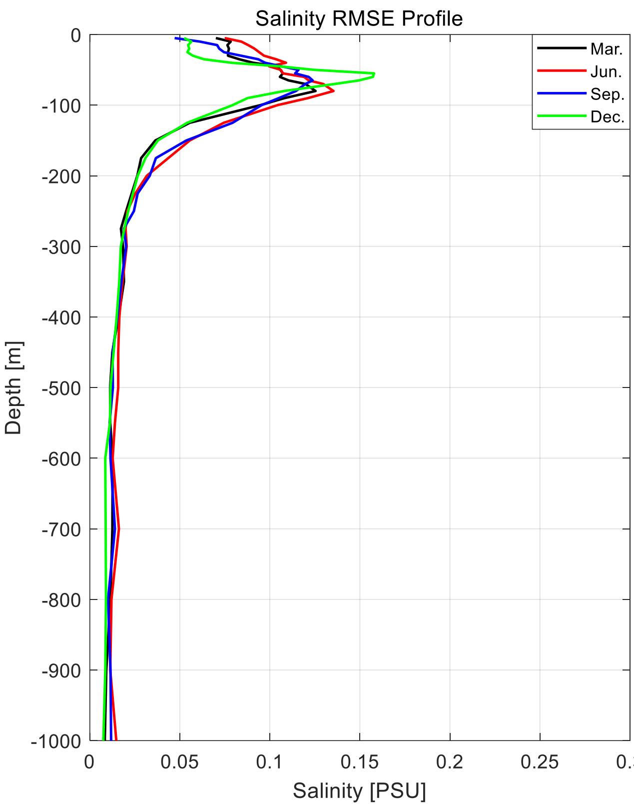


(**a**)

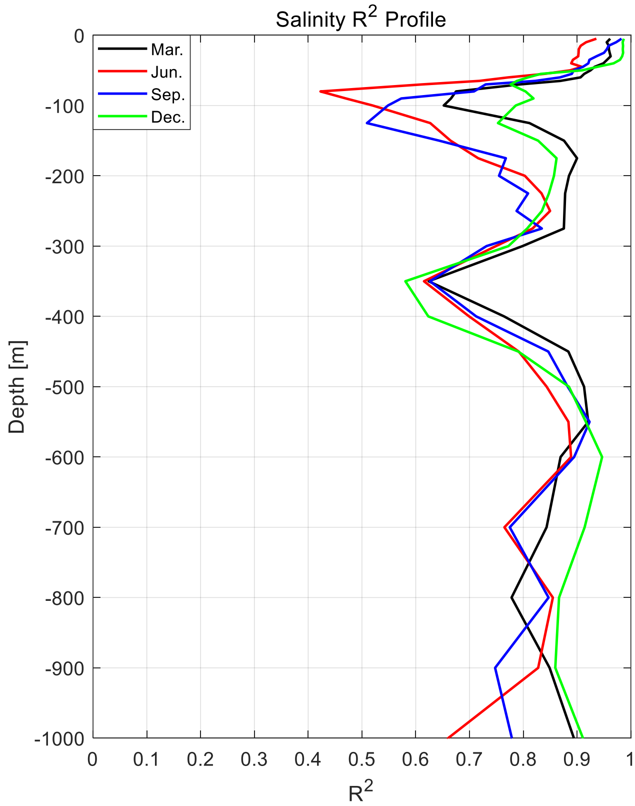


(**b**)

**Figure 20.** RMSE and $R^2$ results of salinity for 2016–2018: (**a**) 3-year average RMSE for 4 months; (**b**) 3-year average $R^2$ for 4 months. The RMSE and $R^2$ count all grid points for each depth layer.

Next, we compare the reconstruction results of the DP-CNN model with that of the traditional CNN model. Table 2 shows the overall RMSE and $R^2$ results for each experimental group. From the experimental results, it can be found that the DP-CNN improves the reconstruction accuracy to a certain extent. The results show that the reconstruction error of the DP-CNN model is generally smaller than that of the traditional CNN model. The DP-CNN model exhibited a lower RMSE of 0.05 PSU, with a 0.01 PSU reduction relative to the CNN model. The evaluation indicator of $R^2$ is almost invalid due to the small order of magnitude for the salinity error. The DP-CNN model also exhibited a higher $R^2$ of 0.86, with an improvement of 0.01 relative to the CNN model.

**Table 2.** RMSE and $R^2$ of reconstructed salinity. The RMSE and $R^2$ in the table are the average values of RMSE and $R^2$ for each layer.

| Evaluation Criteria | Method | March | June | September | December | Mean |
|---|---|---|---|---|---|---|
| RMSE | CNN | 0.06 | 0.06 | 0.05 | 0.05 | 0.06 |
| | DP-CNN | 0.04 | 0.05 | 0.05 | 0.04 | 0.05 |
| $R^2$ | CNN | 0.87 | 0.81 | 0.84 | 0.87 | 0.85 |
| | DP-CNN | 0.88 | 0.81 | 0.84 | 0.89 | 0.86 |

## 4. Discussion

By analyzing the reconstruction results for 2016–2018, it can be found that the errors are usually concentrated in local areas only, while the overall errors are small. The Luzon Strait is a region of more intense fluctuations, where it is vulnerable to mesoscale eddies and Kuroshio. The experimental results show that most of the reconstructed features at Luzon Strait are similar to the ground truth. The only significant error is in the case of typhoon transit.

The transit of a typhoon can cause a decrease in temperature in the upper layers of the ocean, by up to 6 °C. The cold pumping effect of typhoons mixes cold seawater from the deeper layers into the upper layers of the ocean. The stronger the typhoon winds, the more dramatic the upwelling of cold water and the greater the change in upper ocean temperature. The cooling zone will continue to exist for a longer period after the typhoon has passed, but the location may change. Typhoons can cause dramatic changes in the horizontal and vertical structure of the ocean salinity distribution. The pumping effect causes the mixing of high-salinity seawater from the deeper layers into the upper ocean, which leads to an increase in the salinity of the upper layers, and the salinity increase can be around 0.4 PSU. In addition to this, precipitation caused by typhoons can reduce the salinity of the sea surface. Various factors cause the distribution of salinity in the upper ocean during the typhoon transit to deviate from the distribution pattern of historical data, making SS reconstruction complex and difficult.

Artificial intelligence methods tend to be ineffective for unexpected events with large disturbance effects, such as typhoon transits. This is because the training of historical data is generally based on the learning of regular parameters. Although typhoon events can exist in historical data, such extreme values are averaged out in large-sample learning. On the other hand, typhoons are equivalent to random events in big data learning, with irregular paths. Therefore, when typhoon events occur in the reconstruction period, the reconstructed temperature values tend to be higher and the reconstructed salinity values tend to be lower. In contrast, the actual temperature will be lower, and the actual salinity will be higher due to typhoon effects, especially in the upper ocean.

Although the experiments were disturbed by factors such as typhoons, the DP-CNN model showed obvious improvement in the reconstruction accuracy of ST and SS compared with the traditional CNN model through multiple sets of experiments. This indicates that the problem of original information loss has been mitigated by the added skip connection in the CNN model architecture. For ST and SS reconstruction processes, this detailed information may play an important role in reconstruction accuracy.

Taken together, the DP-CNN model can make full use of sea surface information to reconstruct ST and SS, and then achieve the 3D temperature and salinity field. Therefore, the DP-CNN can be an effective method to reconstruct ST and SS. The reconstruction performance of the DP-CNN is significantly better than the traditional CNN model.

To explore the best reconstruction model for the ideal case, only reanalysis information has been used as the data used in this paper. In practice, when using real observations, new disturbances may be introduced due to observation errors and other factors. However, in principle, DP-CNN is a relatively reasonable solution. From this, consider the next steps in our work.

(1) Study the reconstructions of ST and SS at the daily average level.
(2) Research on higher resolution for ST and SS reconstructions.
(3) Using real observations to conduct experiments that are more in line with real conditions.
(4) Develop reconstruction models that can handle the presence of disturbing factors such as typhoons.

We expect that these works will further develop the study of ST and SS reconstruction and contribute to the reconstruction of other ocean elements in the future.

## 5. Conclusions

For unknown ocean information that cannot be directly accessed, it is of great application to use known ocean information to reconstruct unknown ocean information that has relevance to it. Since satellite remote sensing observations cannot provide direct observations of ST and SS, using information from sea surface observations to reconstruct ST and SS has important application value.

To address the problem of detailed information loss in traditional CNN reconstruction models, this paper proposes a solution to this problem by using DP-CNN models. The experimental results fully demonstrate the effectiveness of the DP-CNN model, which has significantly better reconstruction accuracy for ST and SS than the traditional CNN model. The experimental results show that the DP-CNN models have higher reconstruction accuracy than the CNN models, and this proves that DP-CNNs effectively mitigate the loss of detailed information in the CNN models. Compared with the ground truth data, the ST/SS reconstruction results of the DP-CNN model exhibited a high $R^2$ (0.93/0.86) and a low RMSE (around 0.31 °C/0.05 PSU). Therefore, the DP-CNN models can be used as an effective approach to reconstruct ST and SS using sea surface information. Compared with traditional objective analysis methods, DP-CNN utilizes all sea surface grid point parameters to reconstruct one subsurface grid point parameter during the calculation, which indicates that DP-CNNN improves the efficiency of using sea surface parameters. However, it should be noted that this also means a significant increase in computational effort.

The DP-CNN is an effective method for ST and SS reconstruction. We hope that the DP-CNN can help humans to obtain richer and more accurate information on 3D temperature and salinity to better respond to climate change in the future.

**Author Contributions:** Conceptualization, K.M., C.L. and S.Z.; methodology, K.M.; formal analysis, K.M., C.L., S.Z. and F.G.; funding acquisition, C.L. and F.G.; investigation, K.M., C.L., S.Z. and F.G.; resources, C.L., S.Z. and F.G.; software, K.M.; supervision, C.L., S.Z. and F.G.; validation, C.L., S.Z. and F.G.; visualization, K.M.; writing—original draft preparation, K.M.; writing—review and editing, K.M., C.L., S.Z. and F.G. All authors have read and agreed to the published version of the manuscript.

**Funding:** This work was supported by the Heilongjiang Key R&D Program (grant nos. 2022ZX01A15), the National Key R&D Program of China (grant nos. 2022YFE0106400), the National Natural Science Foundation of China (41830964), and Science and Technology Innovation Project of Laoshan Laboratory (grant nos. LSKJ202202200, LSKJ202202201, LSKJ202202202, LSKJ202202203, LSKJ202202204).

**Institutional Review Board Statement:** Not applicable.

**Informed Consent Statement:** Not applicable.

**Data Availability Statement:** Not applicable.

**Acknowledgments:** The authors would like to thank the CMEMS for providing the free data.

**Conflicts of Interest:** The authors declare no conflict of interest.

## References


1. Meyssignac, B.; Boyer, T.; Zhao, Z.; Hakuba, M.Z.; Landerer, F.W.; Stammer, D.; Köhl, A.; Kato, S.; L'ecuyer, T.; Ablain, M.; et al. Measuring global ocean heat content to estimate the earth energy imbalance. *Front. Mar. Sci.* **2019**, *6*, 432. [CrossRef]
2. Johnson, G.C.; Lyman, J.M. Warming trends increasingly dominate global ocean. *Nat. Clim. Chang.* **2020**, *10*, 757–761. [CrossRef]
3. Yang, J.; Gong, P.; Fu, R.; Zhang, M.; Chen, J.; Liang, S.; Xu, B.; Shi, J.; Dickinson, R. The role of satellite remote sensing in climate change studies. *Nat. Clim. Chang.* **2013**, *3*, 875–883. [CrossRef]
4. Wu, X.; Yan, X.-H.; Jo, Y.-H.; Liu, W.T. Estimation of Subsurface Temperature Anomaly in the North Atlantic Using a Self-Organizing Map Neural Network. *J. Atmos. Ocean. Technol.* **2012**, *29*, 1675–1688. [CrossRef]
5. Fiedler, P.C. Surface manifestations of subsurface thermal structure in the California Current. *J. Geophys. Res. Ocean.* **1988**, *93*, 4975–4983. [CrossRef]
6. Carnes, M.R.; Teague, W.J.; Mitchell, J.L. Inference of subsurface thermohaline structure from fields measurable by satellite. *J. Atmos. Ocean. Technol.* **1994**, *11*, 551–566. [CrossRef]
7. Klemas, V. Subsurface and deeper ocean remote sensing from satellites: An overview and new results. *Prog. Oceanogr.* **2014**, *122*, 1–9. [CrossRef]
8. Akbari, E.; Alavipanah, S.K.; Jeihouni, M.; Hajeb, M.; Haase, D.; Alavipanah, S. A review of ocean/sea subsurface water temperature studies from remote sensing and non-remote sensing methods. *Water* **2017**, *9*, 936. [CrossRef]
9. Willis, J.K.; Roemmich, D.; Cornuelle, B. Interannual variability in upper ocean heat content, temperature and thermosteric expansion on global scales. *J. Geophys. Res. Ocean.* **2004**, *109*, C12036. [CrossRef]
10. Gilson, J.; Roemmich, D.; Cornuelle, B.; Fu, L.L. Relationship of TOPEX/Poseidon altimetric height to steric height and circulation in the North Pacific. *J. Geophys. Res. Ocean.* **1998**, *103*, 27947–27965. [CrossRef]
11. Liu, L.; Peng, S.; Wang, J.; Huang, R.X. Retrieving density and velocity fields of the ocean's interior from surface data. *J. Geophys. Res. Ocean.* **2014**, *119*, 8512–8529. [CrossRef]
12. Hurlburt, H.E. The potential for ocean prediction and the role of altimeter data. *Mar. Geod.* **1984**, *8*, 17–66. [CrossRef]
13. Khedouri, E.; Szczechowski, C.; Cheney, R.E. Potential Oceanographic Applications of Satellite Altimetery for Inferring Subsurface Thermal Structure. In Proceedings of the OCEANS '83, San Francisco, CA, USA, 29 August–1 September 1983; pp. 274–280. [CrossRef]
14. Carnes, M.R.; Mitchell, J.L.; De Witt, P.W. Synthetic temperature profiles derived from Geosat altimetry: Comparison with air-dropped expendable bathythermograph profiles. *J. Geophys. Res. Oceans* **1990**, *95*, 17979–17992. [CrossRef]
15. Chu, P.C.; Fan, C.; Liu, W.T. Determination of vertical thermal structure from sea surface temperature. *J. Atmos. Ocean. Technol.* **2000**, *17*, 971–979. [CrossRef]
16. Fischer, M. Multivariate projection of ocean surface data onto subsurface sections. *Geophys. Res. Lett.* **2000**, *27*, 755–757. [CrossRef]
17. Fox, D.N.; Teague, W.J.; Barron, C.N.; Carnes, M.R.; Lee, C.M. The Modular Ocean Data Assimilation System (MODAS). *J. Atmos. Ocean Technol.* **2002**, *19*, 240–252. [CrossRef]
18. Yan, X.H.; Schubel, J.R.; Pritchard, D.W. Oceanic upper mixed layer depth determination by the use of satellite data. *Remote Sens. Environ.* **1990**, *32*, 55–74. [CrossRef]
19. Willis, J.K.; Roemmich, D.; Cornuelle, B. Combining altimetric height withbroadscale profile data to estimate steric height, heat storage, subsurface temperature, and sea-surface temperature variability. *J. Geophys. Res. Ocean.* **2003**, *108(C9)*, 3292. [CrossRef]
20. Guinehut, S.; Dhomps, A.-L.; Larnicol, G.; Le Traon, P.-Y. High resolution 3-D temperature and salinity fields derived from in situ and satellite observations. *Ocean Sci.* **2012**, *8*, 845–857. [CrossRef]
21. Jeong, Y.; Hwang, J.; Park, J.; Jang, C.J.; Jo, Y.-H. Reconstructed 3-D ocean temperature derived from remotely sensed sea surface measurements for mixed layer depth analysis. *Remote Sens.* **2019**, *11*, 3018. [CrossRef]
22. He, Z.; Wang, X.; Wu, X.; Chen, Z.; Chen, J. Projecting Three-dimensional Ocean Thermohaline Structure in the North Indian Ocean from the Satellite Sea Surface Data Based on a Variational Method. *J. Geophys. Res. Ocean.* **2021**, *126*, e2020JC016759. [CrossRef]
23. Reichstein, M.; Camps-Valls, G.; Stevens, B.; Jung, M.; Denzler, J.; Carvalhais, N. Deep learning and process understanding for data-driven Earth system science. *Nature* **2019**, *566*, 195–204. [CrossRef] [PubMed]
24. Garcia-Gorriz, E.; Garcia-Sanchez, J. Prediction of sea surface temperatures in the western Mediterranean Sea by neural networks using satellite observations. *Geophys. Res. Lett.* **2007**, *34*, 11. [CrossRef]
25. Charantonis, A.A.; Badran, F.; Thiria, S. Retrieving the evolution of vertical profiles of chlorophyll-a from satellite observations using hidden Markov models and self-organizing topological maps. *Remote Sens. Enviro.* **2015**, *163*, 229–239. [CrossRef]
26. Friedrich, T.; Oschlies, A. Neural network-based estimates of North Atlantic surface pCO2 from satellite data: A methodological study. *J. Geophys. Res. Ocean.* **2009**, *114*, C03020. [CrossRef]
27. Jo, Y.-H.; Dai, M.; Zhai, W.; Yan, X.-H.; Shang, S. On the variations of sea surface pCO2 in the northern South China Sea: A remote sensing based neural network approach. *J. Geophys. Res. Ocean.* **2012**, *117*, C08022. [CrossRef]
28. Landschützer, P.; Gruber, N.; Bakker, D.C.E.; Schuster, U.; Nakaoka, S.; Payne, M.R.; Sasse, T.P.; Zeng, J. A neural network-based estimate of the seasonal to interannual variability of the Atlantic Ocean carbon sink. *Biogeosciences* **2013**, *10*, 7793–7815. [CrossRef]

29. Li, M.; Gordon, A.L.; Wei, J.; Gruenburg, L.K.; Jiang, G. Multi-decadal timeseries of the Indonesian throughflow. *Dynam. Atmos. Ocean.* **2018**, *81*, 84–95. [CrossRef]
30. Renosh, P.R.; Jourdin, F.; Charantonis, A.A.; Yala, K.; Rivier, A.; Badran, F.; Thiria, S.; Guillou, N.; Leckler, F.; Gohin, F.; et al. Construction of multi-year time-series profiles of suspended particulate inorganic matter concentrations using machine learning approach. *Remote Sens.* **2017**, *9*, 1320. [CrossRef]
31. Ali, M.M.; Swain, D.; Weller, R.A. Estimation of ocean subsurface thermal structure from surface parameters: A neural network approach. *Geophys. Res. Lett.* **2004**, *31*. [CrossRef]
32. Sammartino, M.; Nardelli, B.B.; Marullo, S.; Santoleri, R. An Artificial Neural Network to Infer the Mediterranean 3D Chlorophyll-a and Temperature Fields from Remote Sensing Observations. *Remote Sens.* **2020**, *12*, 4123. [CrossRef]
33. Lu, W.; Su, H.; Yang, X.; Yan, X.H. Subsurface temperature estimation from remote sensing data using a clustering-neural network method. *Remote Sens. Environ.* **2019**, *422*, 213–222. [CrossRef]
34. Han, M.X.; Feng, Y.; Zhao, X.L.; Sun, C.J.; Hong, F.; Liu, C. A Convolutional Neural Network Using Surface Data to Predict Subsurface Temperatures in the Pacific Ocean. *IEEE Access* **2019**, *7*, 172816–172829. [CrossRef]
35. Su, H.; Zhang, T.; Lin, M.; Lu, W.; Yan, X.-H. Predicting subsurface thermohaline structure from remote sensing data based on long short-term memory neural networks. *Remote Sens. Environ.* **2021**, *260*, 112465. [CrossRef]
36. Su, H.; Wu, X.; Yan, X.-H.; Kidwell, A. Estimation of subsurface temperature anomaly in the Indian Ocean during recent global surface warming hiatus from satellite measurements: A support vector machine approach. *Remote Sens. Environ.* **2015**, *160*, 63–71. [CrossRef]
37. Meng, L.; Yan, C.; Zhuang, W.; Zhang, W.; Geng, X.; Yan, X.-H. Reconstructing High-Resolution Ocean Subsurface and Interior Temperature and Salinity Anomalies from Satellite Observations. *IEEE T. Geosci. Remote* **2021**, *60*, 1–14. [CrossRef]
38. Ronneberger, O.; Fischer, P.; Brox, T. U-net: Convolutional networks for biomedical image segmentation. In Proceedings of the International Conference on Medical Image Computing and Computer-Assisted Intervention, Munich, Germany, 5–9 October 2015; pp. 234–241. [CrossRef]